

1 **Interlayer Fusion Bonding of Semi-Crystalline Polymer Composites in Extrusion Deposition**
2 **Additive Manufacturing**

3 Eduardo Barocio¹, Bastian Brenken², Anthony Favaloro¹,
4 R. Byron Pipes¹

5 ¹Composites Manufacturing and Simulation Center, Purdue University,
6 1105 Challenger Ave., West Lafayette, IN 47906. USA

7 ²Composites United e.V. Ottenbecker Damm 12, 21684 Stade. Germany
8 corresponding author: *bpipes@purdue.edu

9 **Abstract**

10 This work focuses on the evolution of interlayer fracture toughness properties of fiber-
11 reinforced, semi-crystalline polymers in the extrusion deposition additive manufacturing
12 (EDAM) process. Further, this work bridges the gap between the additive process conditions
13 (time-temperature history) and the effective layer-to-layer fracture properties developed
14 within a printed component. This is the first step to predict delamination that can occur during
15 printing, during cooling to room temperature after printing, and during service performance
16 of an additively manufactured geometry. A phenomenological model is developed for fusion
17 bonding of semi-crystalline polymer matrix composites by coupling the interdiffusion of
18 polymer chains with the evolution of polymer crystallinity. While the interdiffusion is
19 captured by reptation theory of polymer dynamics, the evolution of crystallinity is modeled
20 by phenomenological crystallization kinetics and crystal melting dynamics. Further, a
21 methodology is developed to determine the critical strain energy release rate, G_{IC} of the
22 interlayer interface and experiments are conducted utilizing the double cantilever beam
23 fracture test geometry. Predictions of G_{IC} as a function of thermal history are compared with
24 experiments.

25 **Keywords:** Fusion Bonding, Extrusion Deposition Additive Manufacturing, Fiber-
26 Reinforced Semi-Crystalline Polymers, Interlayer Fracture Toughness.

27 **1 Introduction**

28 The properties of EDAM manufactured materials of fiber volume fraction greater 20 percent
29 exhibit highly anisotropic mechanical properties due to fiber orientation in flow. The flow of
30 the extrudate from the extruding system into converging zones and cylindrical pathways of
31 the nozzle serve to orient the fibers largely in the print direction and thereby parallel to the
32 interface surface [1]. Interfacial bonding of the layers can limit strengths in the stacking
33 direction by an order of magnitude less than in the print direction. Furthermore, the sequential
34 deposition of layers of molten extrudate onto previously deposited material, at a cooler
35 temperature, can give rise to a thermal gradients and corresponding residual stresses [2, 3].
36 Stresses also develop upon cooling due to the anisotropic thermal expansion of the printed
37 bead. The combination of the strength of the interface and the residual stresses can initiate
38 interlayer debonding, either during the AM process, or during cooling of the geometry after
39 the AM process [4]. Accordingly, this work focuses on modeling and characterizing the
40 fusion bonding process that controls the evolution of interlayer fracture properties in the
41 EDAM process. The model is demonstrated on polyphenylene sulfide (PPS) reinforced with
42 50% weight of carbon fiber (Celanese[®] - Celstran[®] PPS-CF50-01).

43 **2 Fusion Bonding of Semi-Crystalline Polymers**

44 The fusion bonding of fiber-reinforced, thermoplastic polymers in EDAM can be described
45 as a sequence of three steps including: 1) wetting of the substrate, 2) interdiffusion of polymer
46 chains, 3) and solidification with crystallization, for semi-crystalline polymers [5, 6, 7].

47 Figure 1 shows the interaction of two extruded beads during deposition. The first bead (red)
48 is in the molten state as it is extruded upon the previously deposited bead (blue). Next, the
49 compactor squeezes the initially circular cross-section bead (red) into a rectangular cross-
50 section with rounded edges and specified thickness. The compaction action produces the
51 condition of instantaneous wetting of the substrate by the deposited bead. The wetting of the
52 substrate also reduces the thermal resistance between the lower surface of the deposited bead
53 and the surface of the substrate. The second step involves the interdiffusion of polymer chains
54 across the wetted contact area. This phenomenon is thermally driven and requires mobility
55 of polymer chains at the interface. Chain mobility is strongly dependent on temperature and
56 can be restricted by crystallization of polymer chains involved in the crystal phase formation.
57 Thus, there is a competition between onset of crystal formation and polymer chain mobility.
58 The third step is the growth of semi-crystalline structures across the interface to enhance the
59 interlayer properties [8, 9, 10].

60 To develop crystallinity across an interface, the substrate must be either initially in the
61 amorphous state or local melting of the semi-crystalline polymer substrate must occur. When
62 either of the conditions is met, interdiffusion of polymer chains is allowed. During
63 crystallization, polymer crystals incorporate the polymer chains from both bonding volumes,
64 as shown schematically in Figure 1. Thus, the proposed model assumes that the semi-
65 crystalline structure developed across the interface depends on the degree of molecular
66 interdiffusion achieved prior to the onset of crystallization. Further, the kinetics of the
67 interdiffusion process is assumed to control the rate of development of interlayer fracture
68 properties.

69 A pathological mechanism occurs when the bead is deposited onto a significantly cooler
70 substrate without melting of the substrate. In this case, a large degree of supercooling
71 develops at the lower surface of the deposited bead. Under this scenario, nucleation and
72 growth of crystallinity from the interface into the volume of the bead is thereby promoted,
73 while crystal growth across the interface is prevented.

74 The description of these two mechanisms at the interface is supported by the experimental
75 observations from the non-isothermal bonding experiments performed with different
76 polymers by Bourban et al. [6], Smith et al. [9], Plummer et al. [10], and Zanetto et al. [11].
77 Further, the study of Groupe et al. [12] has shown the effects of crystallinity on fracture
78 toughness for high cooling rates developed in thermoplastic prepreg fiber tape placement.

79 **3 Bonding Model**

80 In the following, a phenomenological model is developed for fusion bonding of semi-
81 crystalline polymer matrix composites that combines the interdiffusion of polymer chains
82 with the evolution of crystallinity. While the interdiffusion of polymer chains is captured
83 with a model derived from the reptation theory of polymer dynamics, the evolution of
84 crystallinity is modeled by phenomenological crystallization and crystal melting kinetics.
85 The degree of bonding is defined as the ratio of the interlayer, mode-I, strain energy release
86 rates, $G_{IC}(t)$ to $G_{IC\infty}$; where, $G_{IC}(t)$ reflects strain energy release rate corresponding to the
87 actual thermal history of the interface and $G_{IC\infty}$ is that of the host, fiber-reinforced
88 thermoplastic polymer (with the appropriate fiber orientation state). Thus, $D_b(t)$
89 $= G_{IC}(t)/G_{IC\infty}$. Values for $G_{IC}(t)$ and $G_{IC\infty}$ are determined through mode-I fracture tests of
90 additively manufactured Double Cantilever Beam (DCB) geometries as described later.

91 **3.1 Interdiffusion of Polymer Chains**

92 The reptation theory of polymer dynamics developed by De Gennes [13, 14] serves as the
93 basis for determining the time evolution of the polymer interdiffusion process. Utilizing
94 arguments of the reptation theory, the welding time, t_w can be defined as the time required
95 for the polymer chain to escape from a confining tube formed by topological constraints
96 surrounding the polymer chain. Such constraints are introduced by entanglements with
97 neighboring polymer chains and by rigid constraints like reinforcing fibers or particles.
98 Interdiffusion is assumed to be complete once a significant portion of the polymer chain
99 abandons its confining tube [8, 15]. Thus, the kinetics of the bonding process is polymer type
100 and time-temperature process dependent since the welding time follows a power-law
101 dependence on the molecular weight and an exponential dependence on the temperature [16].
102 Utilizing the reptation theory, multiple models have been derived to describe the evolution
103 of interdiffusion with time and under non-isothermal conditions [15, 17]. These models
104 provide valuable relationships derived from polymer dynamics and can be utilized to make
105 quantitative predictions of the interlayer fracture toughness properties.

106 **3.2 Polymer Crystallization and Melting**

107 Polymer crystallization is a reversible physical transformation occurring as semi-crystalline
108 polymers are cooled from the processing temperature to room temperature. It consists of two
109 sequential steps: crystal nucleation and crystal growth. Ordering of polymer chains in a
110 crystalline structure produces shrinkage and releases thermal energy (exothermic heat).
111 Homogenous and heterogeneous nucleation occur in fiber-reinforced, semi-crystalline
112 polymers. While for the homogenous case, nuclei develop and grow primarily in the form of

113 spherulitic structures in the bulk polymer, in the heterogonous case, nuclei develop on the
 114 surface of heterogeneities, like fiber surfaces, and grow into columnar structures [18]. A
 115 phenomenological model of polymer crystallization developed by Velisaris and Seferis [19]
 116 has been adopted to capture the kinetics in highly non-isothermal conditions developed in
 117 EDAM. The kinetics of each mechanism is given as a function, $F_i, i = 1,2$, and the
 118 contribution of each mechanism to the degree of crystallinity, $X(T, t)$, is weighted by the
 119 factors, $w_i, i = 1,2$, with $w_1 + w_2 = 1$. The product of the weighted sum of the two
 120 crystallization mechanisms and the maximum degree of crystallinity, X_∞ , yields the degree
 121 of crystallinity as given by Equation 1.

$$X(T, t) = X_\infty(w_1F_i + w_2F_i) \quad (1)$$

122 The functions $F_i, i = 1,2$, describing the kinetics of each crystallization mechanism are
 123 given by Equation 2.

$$F_i = 1 - \exp \left\{ -C_{1_i} \int_{t_{xtal}}^T \right. \\ \left. \cdot \exp \left[\frac{-C_{2_i}}{(T - T_g + T_{c_i})} - \frac{C_{3_i}}{(T(T_{m_i} - T)^2)} \right] n_i \tau^{n_i-1} d\tau \right\} \quad (2)$$

$$t_{xtal} \in \{\bar{t} \leq t \mid T < T_m^*\}$$

124 Where the term C_{1_i} relates the dependence crystallization rate on temperature, while C_{2_i}
 125 relates to the dependence of the crystal growth on temperature, and C_{3_i} relates to the enthalpy
 126 of nucleation. The integration domain, t_{xtal} , allows for the calculation of crystallinity over

127 multiple intervals of time when melting occurs. The temperatures T , T_g and T_{m_i} correspond
128 to the temperature of the process, the glass transition temperature, and the melting
129 temperature of the polymer, respectively. The parameters, n_i , correspond to the Avrami
130 coefficients of each of the crystallization mechanisms. The parameters C_{1_i} , C_{2_i} , and C_{3_i} , ($i =$
131 $1,2$), and the temperatures T_{c_i} , ($i = 1,2$), are determined by fitting the model to crystallization
132 kinetics data obtained from non-isothermal crystallization experiments carried out at cooling
133 rates relevant for the EDAM process. The crystallization kinetics of the CF-PPS used in this
134 work was characterized through differential scanning calorimetry (DSC). Since isothermal
135 crystallization is known to occur between 519 K and 531K for the PPS in the current study
136 [20], isothermal crystallization experiments at temperatures in the range of 519 K to 531 K
137 were used to determine the two Avrami coefficients; whereas, non-isothermal crystallization
138 experiments carried out at cooling rates between 30 K/min and 10400 K/min were used to
139 fit the model. Data for cooling rates of up to 190 K/min was extracted directly from DSC
140 experiments while data for the highest cooling rates was obtained by quenching samples and
141 then characterizing the cold crystallization event to determine the amount of crystallinity
142 developed during quenching. The experimental procedures and characterized model
143 parameters can be found elsewhere [20]. A maximum degree of crystallinity of 84% was
144 achieved in the CF-PPS considering a heat of crystallization of 76 J/g for a completely
145 crystallized material [21].

146 The melting behavior of polymer crystals depends primarily on the size distribution of the
147 lamella structures developed as the polymer is cooled from the melt [18]. Melting is described

148 with a phenomenological model that considers a fixed distribution of lamellar thicknesses
 149 with a sharpness factor, k_{mb} , and a distribution factor, d , as given by Equation 3 [22].

$$\frac{dX_{vc}}{dT} = k_{mb} \{ \exp[-k_{mb}(T - T_c)] \} \cdot (1 + (d - 1) \exp[-k_{mb}(T - T_c)])^{\frac{d}{1-d}} \quad (3)$$

150 The temperature T_c corresponds to that of the maximum heat flow amplitude as characterized
 151 in melting experiments utilizing DSC. The melting behavior characterized with DSC at
 152 different heating rates is used to fit k_{mb} and d in the melting model [2].

153 The evolution of the degree of crystallinity was determined by the models for crystallization
 154 kinetics and melting coupled through a temperature condition as given by Equation 4. While
 155 the melting model dominates the evolution of crystallinity for temperatures above the onset
 156 temperature of melting T_m^* , the crystallization kinetics model dominates for temperatures
 157 below T_m^* .

$$X = \begin{cases} T > T_m^*, & X(T) - \text{Melting} \rightarrow \text{Equation 3} \\ T \leq T_m^*, & X(T, t) - \text{Crystallization} \rightarrow \text{Equation 1} \end{cases} \quad (4)$$

$$X \in [0 \ 1]$$

158 T_m^* corresponds to the lowest value of the temperature range over which melting occurs
 159 according to the melting model given by Equation 3. This temperature corresponds to
 160 523.15 K for the CF-PPS used in this work. Finally, the integrals in the crystallization
 161 kinetics model (Equation 2) must be updated to reflect the change in degree of crystallinity
 162 when melting occurs.

163 3.3 Degree of Bonding

164 The degree of bonding, $D_b(t)$ is defined in a range from zero to unity. Zero corresponds to
165 non-bonding and unity to full bonding, where the fracture properties of the host composite
166 are developed (*i. e.*, $G_{IC}(t) = G_{IC\infty}$). The model developed by Yang and Pitchumani [15]
167 was extended to describe the non-isothermal evolution of interdiffusion as a function of time,
168 temperature, and crystallinity. The time during which interdiffusion occurs is limited by the
169 development of crystallinity as given by Equation 5. To capture the effect of crystallization
170 on interdiffusion, the integral is evaluated only in the time domain $t_I(X)$ wherein the degree
171 of crystallinity X is less than a critical degree of crystallinity X^{crit} . X^{crit} is defined as the
172 degree of crystallinity corresponding to termination of polymer chain interdiffusion.

$$D_b(t, T) = \frac{G_{IC}(t)}{G_{IC\infty}} = \left[\int_{t_I(X)} \frac{1}{t_w(T)} d\tau \right]^{\frac{1}{2}}, t_I(X) \in \{\bar{t} \leq t \mid X < X^{crit}\} \quad (5)$$

173 This definition allows the integration to be performed over multiple time segments when
174 remelting occurs as multiple layers are deposited. The total time where the degree of
175 crystallinity is less than the critical value is termed the time to crystallize, $t_c = \int_{t_I(X)} d\tau$. A
176 relative low degree of crystallinity can be assumed to deter the interdiffusion of polymer
177 chains (*i.e.*, $X^{crit} = 5\%$). This assumption was made to account for the rapid decrease in
178 diffusivity (or increase in viscosity) that results from the development of crystallinity, which
179 has been investigated experimentally by other groups [23]. The dependence of $t_w(T)$ on
180 temperature is captured through an Arrhenius expression as given by Equation 6.

$$t_w(T) = A \cdot \exp\left(\frac{E_A}{RT}\right) \quad (6)$$

181 Where A is a pre-exponential factor, E_A is an activation energy, and R is the universal gas
182 constant. Multiple techniques can be used to characterize $t_w(T)$ as a function of temperature
183 including bonding experiments, small angle oscillatory shear rheology, stress relaxation
184 experiments and healing experiments [24, 25, 26, 27]. $t_w(T)$ was characterized through non-
185 isothermal bonding experiments due to the presence of fibers and the highly non-isothermal
186 conditions developed in the EDAM process.

187 **4 Degree of Bonding Predictions and Experiments**

188 The first step to predict the degree of bonding is to characterize the welding time $t_w(T)$ as a
189 function of temperature. Non-isothermal bonding experiments consisting of DCB mode-I
190 fracture tests and time-temperature history predictions for the printed DCB specimens were
191 used to characterize the welding time of CF-PPS. The fracture tests provided values for the
192 degree of bonding whereas the time-temperature history provided the process history that
193 produced the corresponding degree of bonding. In the following, the methods for
194 characterizing the degree of bonding and the time-time history predictions are presented.

195 **4.1 Experimental Characterization of Degree of Bonding**

196 The non-isothermal bonding experiments consisted of printing DCB specimens under
197 different process conditions that led to different temperature and crystallinity time histories.
198 Thus, DCBs with different degrees of bonding at the plane of crack propagation were
199 developed. The process conditions varied in the bonding experiments were the temperature
200 of the build plate and the duration of a dwell time between the third and fourth layers that

201 forms the plane for crack propagation in a DCB. Table 1 lists seven combinations of printing
202 conditions used and an eighth condition corresponding to a heat-treated panel to determine
203 the fracture toughness of the host composite material. The reasoning for choosing the
204 temperatures for Table 1 can be summarized as follows: The two lower temperatures were
205 chosen to be above the glass transition temperature of the polymer ($\sim 363\text{ K}$), where bonding
206 is limited by the rapid development of crystallinity. Parts printed on build plate temperatures
207 below the glass transition temperature result in weak bonding between the first couple of
208 layers, thereby causing the parts to delaminate in that region during the printing process.
209 Furthermore, 413 K was the maximum build plate temperature used in other types of
210 substrates such as thin sheets ($1.5 - 3\text{ mm}$ in thickness) made from polycarbonate
211 ($T_g \sim 413\text{ K}$). The temperature of 488 K was chosen because it is a typical build plate
212 temperature used for printing with CF-PPS. Finally, the maximum temperature of 523 K was
213 chosen based on the maximum capacity of the system used for printing.

214 The Composites Additive Manufacturing Research Instrument (CAMRI) [20, 28], was
215 utilized to print DCB specimens with CF-PPS. CAMRI is fed with pelletized material and is
216 equipped with a tamper that provided compaction of the beads extruded through a nozzle
217 with an orifice diameter of 3.175 mm .

218 DCB specimens were fabricated with approximate dimensions of 25.0 mm in width, 7.8 mm
219 in thickness, and 150 mm in length, in accordance with the ASTM D5528 test standard [29].
220 The thickness of the specimens was chosen to accommodate the relatively low bending
221 strength of the printed material. The elastic modulus of the CF-PPS in the print direction had
222 been characterized as 24.7 GPa [20]. It was verified through requirements in the ASTM

223 D5528 standard that the thickness used in the DCB specimen provided adequate bending
224 stiffness. Figure 2 summarizes the procedure followed for preparing DCB specimens. In the
225 first step, rectangular panels with dimensions of 100 *mm* by 180 *mm* and with six beads in
226 the thickness direction were printed with beads oriented parallel to the beam. Process
227 conditions for printing the panels in CAMRI are listed in Table 2. The void content inside
228 the printed beads (intra-bead voids) was determined to be in the range of 3 to 4%, while the
229 inter-bead voids were eliminated by the compactor.

230 An initial crack was introduced on one side of the specimens by placing a piece of polyimide
231 film (25 μm UPILEX[®] - Ube Industries Ltd.) during the printing process of the panels.
232 CAMRI was programmed to move to a predefined safe position within the dwell time,
233 thereby allowing for the precise placement of the polyimide film. The printing process was
234 automatically resumed once the dwell time was completed, and three additional layers were
235 printed onto the previously printed substrate. Once the printing process was completed, the
236 panels remained for five minutes on the heated build plate and then were removed from the
237 build plate and allowed to cool to the room temperature. To create DCB specimens with the
238 fracture toughness of the host fiber-reinforced polymer composite, ($G_{IC\infty}$), printed DCB
239 specimens (DCB-523-10-HT) were heat treated for approximately 15 minutes at the process
240 temperature of the CF-PPS (573.15 *K*) to allow further interdiffusion of polymer chains. The
241 duration of the heat treatment was chosen to develop a uniform temperature across the sample
242 while exceeding the welding time reported in the literature for a similar polymer [30]. No
243 dimensional changes or geometrical distortions were observed after the heat-treatment of the
244 samples.

245 In a second step, piano hinges were adhesively bonded to the panel with a urethane adhesive
246 (Lord-7542) following procedures recommended by the manufacturer for surface preparation
247 and bonding. The plates with bonded piano hinges were then precisely cut into three DCB
248 specimens utilizing a CNC controlled waterjet cutting system. The edges of the printed panel
249 were discarded to avoid variations in the degree of bonding due to different cooling
250 conditions around the edges of the panels. Specimens were dried in a polymer pellet dryer
251 for 24 hours at 335.15 K (below the T_g of the polymer). Specimen dimensions and initial
252 crack lengths, a_0 , were recorded after drying.

253 The DCB fracture tests were conducted in a universal testing machine (MTS[®]-810) equipped
254 with a 5 KN load cell and under fixed grip conditions to attain stable crack propagation. A
255 loading rate of 2 *mm/min* was used for opening the DCB whereas an unloading rate of
256 10 *mm/min* was used for closing the DCB [29]. A traveling optical microscope (Leica[®]
257 S6D) equipped with a digital camera (PixeLINK[®] Model PL-B776) was used to record the
258 extension of the crack tip and thereby, crack length during the fracture test. Three loading
259 cycles were performed per specimen wherein the crack was extended by approximately 25
260 mm. Four crack extensions per loading cycle including the visual onset of the crack extension
261 were extracted from images recorded during the fracture test. Figure 3-A shows an example
262 of the load-displacement curve for one of the DCB-488-5 specimens and indicates points of
263 crack initiation and crack propagation with blue and black asterisks, respectively.

264 Three methods were utilized to determine G_{IC} , namely the Compliance Calibration (CC)
265 method, the Modified Beam Theory (MBT) method, and the Modified Compliance
266 Calibration (MCC) method [29, 31]. Further, G_{IC} was determined at the points of crack

267 initiation and propagation. Figure 3-B shows the delamination resistance curve created for
268 one of the DCB-488-5 specimens and with G_{IC} determined through the three methods. The
269 fluctuations in G_{IC} observed along the crack length can be attributed to a circuitous crack
270 propagation path developed around the plane of crack propagation in the DCB. The degree
271 of bonding was determined from the values for G_{IC} obtained with the CC method since this
272 yielded the most conservative (lowest) values and the smallest standard deviation of the three
273 methods.

274 A mean value for G_{IC} was determined for each of the bonding conditions using all the
275 corresponding measurements. Since the mean G_{IC} for the heat-treated specimens was
276 practically the same as that for the DCB-523-10 specimens, the mean G_{IC} of the latter was
277 considered as the value for a completely bonded joint for this material system. Finally, the
278 mean and the standard deviation of the degree of bonding were computed for all the printing
279 conditions and results are summarized in Table 3.

280 **4.2 Inspection of Crack Propagation Path**

281 The crack propagation path developed in DCB specimens with significantly different degree
282 of bonding were compared. Sections of DCBs were cut near the crack tip to examine the
283 crack propagation path at the edge of the specimen. Standard procedures for mounting and
284 preparing the specimens for inspection in a scanning electron microscope (SEM) were
285 followed. The surface of the specimens was sputter coated with a thin film of gold/palladium
286 to allow for electrostatic discharge. A Scanning Electron Microscope (SEM) (Quanta 650
287 FEG) equipped with a back-scattered electrons detector was utilized to scan the edge of the
288 DCB specimens. Figure 4 shows SEM micrographs of the two bonding conditions that

289 yielded a D_b close to one and the lowest D_b , DCB-488-5 and DCB-393-10, respectively. The
290 fibers in the samples were dominantly oriented along the print direction. The path of crack
291 propagation is indicated with a yellow dotted line in both figures. Figure 4-A shows a clean
292 and straight crack propagation path developed in the specimen printed with the conditions
293 DCB-393-10. The straight crack propagation path suggests that crystallinity did not develop
294 across the interface and instead, polymer crystals likely nucleated from the surface of the
295 printed substrate. The crack tip is not shown in Figure 4-A since this specimen was
296 completely delaminated after the fracture test. Further, the sample was not clamped to avoid
297 altering the crack surfaces, both sides were simply held together while mounting the
298 specimen in epoxy resin. In contrast, Figure 4-B shows a circuitous crack propagation path
299 developed in the specimen printed with the conditions of DCB-488-5. This path indicates
300 the presence of a semi-crystalline structure developed across the interface. The bright region
301 ahead of the crack tip in Figure 4-B is a void entrapped in the printed material.

302 Figure 5 shows a closer view of the crack propagation path developed in the specimen printed
303 with the DCB-488-5 conditions. This micrograph reveals multiple spherulitic structures
304 located on both sides of the crack propagation path. Further, it seems as though the crack
305 found the least resistance path to propagate across the impingement of adjacent spherulitic
306 structures in the region near the crack tip.

307 **4.3 Transient Heat Transfer Analysis**

308 To determine the time-temperature histories at the layer-to-layer interface, a transient heat
309 transfer analysis of the printing process of the panel was carried out for each of the bonding
310 conditions in Abaqus[®] Standard [32]. Printed beads were represented with a voxel mesh with

311 three by four linear solid elements type DC3D8 along the height and width, respectively. The
312 heat transfer analysis considered orthotropic heat conduction, radiative and convective heat
313 losses, the heat removed by the compactor, and the exothermic heat due to crystallization. A
314 detailed description of the transient heat transfer analysis can be found elsewhere [2, 20, 28].
315 Furthermore, experimental validation of the heat transfer analysis has been carried out by the
316 author [28], but is not discussed in the present work. Average ambient and process conditions
317 used in the transient heat transfer analysis are listed in Table 4. Figure 6 shows an example
318 of the temperature field developed during the printing process of the panel labeled as
319 DCB-413-10.

320 Temperature-crystallinity-time histories were extracted for each of the printing conditions at
321 the interlayer region as predicted in the finite-element model. Figure 7 shows the temperature
322 time histories extracted after the rapid temperature drop that occurred upon activating the
323 element and until the time t_c where the degree of crystallinity reached the critical value,
324 $X^{crit} = 5\%$. The effect of the build plate temperature was found to be more significant as
325 compared to the dwell time as shown by the temperature profiles. This result follows from
326 the dominance of heat conduction through the thickness for the relatively thin panels printed
327 onto the build plate surface.

328 **4.4 Characterization of Welding Time**

329 Following the experimental characterization of the degree of bonding and the prediction of
330 the time-temperature histories, the activation energy, and the pre-exponential factor in
331 Equation 6 were characterized by minimizing a quadratic loss function defined in terms of
332 the experimental degree of bonding and the bonding model predictions. That is to say that

333 the experimental degree of bonding corresponds to the bonding developed within the time to
334 crystallize. A non-linear least squares optimization tool available in Matlab[®] was used to
335 characterize the activation energy and the pre-exponential factor utilizing the six
336 experimental measurements of the degree of bonding listed in Table 3 and the corresponding
337 temperature time histories shown in Figure 7. The activation energy and the pre-exponential
338 factor are listed in Table 5.

339 Figure 8 shows the welding time as a function of temperature for CF-PPS. This plot indicates
340 that the time necessary to develop the maximum degree of bonding around the melt
341 temperature (580 K) is only around five seconds. It should be recognized that the
342 characterization of this bonding model is non-local since the degree of bonding developed at
343 an interface between two adjacent layers is resolved from the temperature and crystallinity at
344 an integration point located at a relatively small distance above the interface.

345 **4.5 Interlayer Bonding Predictions**

346 The fusion bonding model (Equation 5) was implemented in a UMATHT subroutine in
347 Abaqus[®] for predicting the degree of bonding in printing simulations carried out with the
348 Additive3D EDAM process simulation workflow [2, 32]. This subroutine is called at each
349 material point and every global iteration. The information passed into the subroutine is used
350 to compute the evolution of the degree of bonding and crystallinity in each increment of the
351 finite element solution. While the evolution of crystallinity is defined by Equations 1 through
352 4 as a function of time and temperature, the evolution of the degree of bonding is coupled
353 with the temperature and crystallinity as given by Equation 5. Further details on the

354 implementation of these models in the UMATHT subroutine can be found elsewhere [33,
355 34].

356 To verify the predictions of the fusion bonding model, the printing process of the panels used
357 for preparing DCB specimens was simulated. The event series used previously for the
358 characterization of the temperature and crystallization time histories were used to perform
359 the bonding simulations. Figure 9 shows the field of degree of bonding developed at a plane
360 coincident with the integration points where bonding calculations are carried out for two of
361 the bonding experiments. In both cases, the degree of bonding is relatively uniform towards
362 the center of the plate. However, gradients in the degree of bonding developed towards the
363 edges of the plate. These gradients resulted from variations in cooling and crystallization
364 histories developed from the center of the plate to the edges. Furthermore, these gradients
365 also indicate the directions with the least resistance for crack propagation in the plane.

366 A quantitative verification was conducted by extracting the degree of bonding at relevant
367 integration points located along two paths in the X (printing) and Y (transverse) directions.
368 These paths were centered along the width and the length of the printed panel. The mean of
369 the degree of bonding was computed from data points collected along each path and within
370 50 mm from the edges of the panel. Figure 10 compares the mean degree of bonding predicted
371 in the EDAM process simulation to the experimentally determined D_b . The blue error bars in
372 the experimental data indicate one standard deviation from the mean value.

373 Acceptable correlation between experimentally measured and predicted degrees of bonding
374 was obtained for five of the conditions as shown in Figure 10, however, the prediction for
375 the DCB-413-10 printing condition was significantly overestimated. The experimental

376 measurements for this bonding condition also yielded the most significant coefficient of
377 variation (standard deviation relative to the mean) of the six bonding conditions.
378 Furthermore, a clean and straight crack propagation path shown in Figure 4-A of the appendix
379 indicated that crystallinity did not grow through the plane of crack propagation, but it rather
380 nucleated and grew from the interface. As a result, the fracture response of this bonding
381 condition was governed by secondary bonding, namely mechanical interlocking through the
382 roughness of the printed substrate and crystal nucleation at the interface. Although a
383 relatively low degree of bonding (<0.5) should be avoided in a printed part, mechanisms of
384 secondary bonding deserve further research.

385 The degree of crystallinity developed across the printed panels was predicted with the process
386 simulation and confirmed experimentally through DSC. The maximum degree of crystallinity
387 of 0.84 was achieved in all the printed panels, as confirmed by DSC measurements, thereby
388 confirming that the experimental measurements of the degree of bonding were not affected
389 by variations in crystallinity within the printed panels.

390 **5 Conclusions**

391 The mechanisms for fusion bonding of fiber reinforced, semi-crystalline polymers were
392 presented in the context of the EDAM process where wetting is not the rate-limiting step for
393 bonding. This results from the use of a compactor that consolidates the beads of molten
394 material onto the printed substrate. Further, the development of crystallinity across the
395 interface of adjacent layers has been shown to be of paramount importance to develop
396 interlayer fracture properties under the highly non-isothermal conditions developed in the
397 EDAM process. Interactions of polymer chain diffusion and crystallization during cooling

398 and solidification have been shown to be key to development of interface strain energy
399 release rate.

400 A non-isothermal fusion bonding model for semi-crystalline polymer matrix composites was
401 developed by coupling a model for interdiffusion of polymer chains with the evolution of
402 crystallinity. This coupling was shown to capture the effect of crystallization in precluding
403 the mobility of polymer chains. The degree of bonding predicted with this model provides
404 the ratio of the G_{IC} developed between adjacent layers to the $G_{IC\infty}$ measured from a
405 completely bonded joint of the same material system. The fusion bonding model was
406 exercised through the combination of non-isothermal DCB bonding experiments and
407 predictions of the temperature and crystallinity time histories obtained from a transient heat
408 transfer analysis.

409 Comparison of the predictions of degree of bonding to experimental results was carried out
410 by simulating the EDAM process of the panels utilized for preparing DCB specimens.
411 Predictions were in good agreement with the experimental measurements except for the
412 condition where crystallization did not occur across the interface. Finally, the fusion bonding
413 model developed has application to delamination that can occur during printing, during
414 cooling to room temperature after printing, and during service performance of an additively
415 manufactured geometry.

416 **6 References**

417

- [1] B. P. Heller, D. E. Smith and D. A. Jack, "Effects of extrudate swell and nozzle geometry on fiber orientation in Fused Filament Fabrication nozzle flow," *Additive Manufacturing* , Vols. 12, Part B, pp. 252-264, 2016.
- [2] B. Brenken, E. Barocio, A. Favaloro, V. Kunc and R. B. Pipes, "Development and validation of extrusion deposition additive manufacturing process simulations," *Additive Manufacturing*, vol. 25, pp. 218-226, 2019.
- [3] A. El Moumen, M. Tarfaoui and K. Lafdi, "Modelling of the temperature and residual stress fields during 3D printing of polymer composites," *The International Journal of Advanced Manufacturing Technology*, Jun 2019.
- [4] J. Beuth and S. Narayan, "Residual stress-driven delamination in deposited multi-layers," *International Journal of Solids and Structures*, vol. 33, no. 1, pp. 65-78, 1996.
- [5] R. P. Wool, B.-L. Yuan and O. J. McGarel, "Welding of polymer interfaces," *Polymer Engineering & Science*, vol. 29, no. 19, pp. 1340-1367, 1989.
- [6] P.-E. Bourban, N. Bernet, J.-E. Zanetto and J.-A. E. Månson, "Material phenomena controlling rapid processing of thermoplastic composites," *Composites Part A: Applied Science and Manufacturing*, vol. 32, no. 8, pp. 1045-1057, 2001.
- [7] R. P. Wool and K. M. O'Connor, "A theory crack healing in polymers," *Journal of Applied Physics*, vol. 52, pp. 5953-5963, 1981.

- [8] R. P. Wool, *Polymer interfaces: structure and strength*, Hanser, 1995.
- [9] G. D. Smith, C. J. Plummer, P.-E. Bourban and J.-A. E. Månson, "Non-isothermal fusion bonding of polypropylene," *Polymer*, vol. 42, no. 14, pp. 6247-6257, 2001.
- [10] C. J. G. Plummer, P.-E. Bourban, J.-E. Zanetto, G. D. Smith and J.-A. E. Månson, "Nonisothermal fusion bonding in semicrystalline thermoplastics," *Journal of Applied Polymer Science*, vol. 87, no. 8, pp. 1267-1276, 2003.
- [11] J.-E. Zanetto, C. J. G. Plummer, P.-E. Bourban and J.-A. E. Månson, "Fusion bonding of polyamide 12," *Polymer Engineering & Science*, vol. 41, no. 5, pp. 890-897, 2001.
- [12] W. J. B. Grouve, G. V. Poel, L. L. Warnet and R. Akkerman, "On crystallisation and fracture toughness of poly(phenylene sulphide) under tape placement conditions," *Plastics, Rubber and Composites*, vol. 42, no. 7, pp. 282-288, 2013.
- [13] P. De Gennes and L. Leger, "Dynamics of entangled polymer chains," *Annual Review of Physical Chemistry*, vol. 33, no. 1, pp. 49-61, 1982.
- [14] P.-G. De Gennes, "Reptation of a polymer chain in the presence of fixed obstacles," *The journal of chemical physics*, vol. 55, no. 2, pp. 572-579, 1971.
- [15] F. Yang and R. Pitchumani, "Nonisothermal healing and interlaminar bond strength evolution during thermoplastic matrix composites processing," *Polymer Composites*, vol. 24, no. 2, pp. 263-278, 2003.

- [16] M. Rubinstein and R. H. Colby, *Polymer physics*, vol. 23, Oxford University Press New York, 2003.
- [17] L. J. Bastien and J. W. Gillespie, "A non-isothermal healing model for strength and toughness of fusion bonded joints of amorphous thermoplastics," *Polymer Engineering & Science*, vol. 31, pp. 1720-1730, 1991.
- [18] E. Piorkowska and G. C. Rutledge, *Handbook of polymer crystallization*, John Wiley & Sons, 2013.
- [19] C. N. Velisaris and J. C. Seferis, "Crystallization kinetics of polyetheretherketone (peek) matrices," *Polymer Engineering & Science*, vol. 26, pp. 1574-1581, 1986.
- [20] B. Brenken, *Extrusion Deposition Additive Manufacturing of Fiber Reinforced Semi-crystalline Polymers*, West Lafayette: Ph.D. Dissertation, 2017.
- [21] J. Kenny and A. Maffezzoli, "Crystallization kinetics of poly (phenylene sulfide)(PPS) and PPS/carbon fiber composites," *Polymer Engineering & Science*, vol. 31, no. 8, pp. 607-614, 1991.
- [22] A. Greco and A. Maffezzoli, "Statistical and kinetic approaches for linear low-density polyethylene melting modeling," *Journal of Applied Polymer Science*, vol. 89, no. 2, pp. 289-295, 2003.

- [23] R. Pantani, V. Speranza, G. Titomanlio and R. Pantani, "Simultaneous morphological and rheological measurements on polypropylene: Effect of crystallinity on viscoelastic parameters," *Journal of Rheology*, vol. 59, no. 2, pp. 377-390, 3 2015.
- [24] R. P. Wool and K. M. O'Connor, "Time dependence of crack healing," *Journal of Polymer Science: Polymer Letters Edition*, vol. 20, no. 1, pp. 7-16, 1982.
- [25] P. Dara and A. Loos, "Thermoplastic Matrix Composite Processing Model, Virginia Polytechnic Institute," 1985.
- [26] M. Tirrell, "Polymer Self-Diffusion in Entangled Systems," *Rubber Chemistry and Technology*, vol. 57, no. 3, pp. 523-556, 1984.
- [27] K. Jud and H. H. Kausch, "Load transfer through chain molecules after interpenetration at interfaces," *Polymer Bulletin*, vol. 1, no. 10, pp. 697-707, 1979.
- [28] E. Barocio, Fusion Bonding of Fiber Reinforced Semi-Crystalline Polymers in Extrusion Deposition Additive Manufacturing, West Lafayette: Ph.D. Dissertation, 2018.
- [29] ASTM, *ASTM D5528 - Standard Test Method for Mode I Interlaminar Fracture Toughness of Unidirectional Fiber-Reinforced Polymer Matrix Composites*, 2013.
- [30] W. Grouve, L. Warnet, B. Rietman, H. Visser and R. Akkerman, "Optimization of the tape placement process parameters for carbon-PPS composites," *Composites Part A: Applied Science and Manufacturing* , vol. 50, pp. 44-53, 2013.

- [31] L. A. Carlsson, D. F. Adams and R. B. Pipes, Experimental characterization of advanced composite materials, CRC press, 2014.
- [32] "Abaqus Online Documentation Server," Dassault Systemes, 2017. [Online]. Available: <http://50.16.225.63/>. [Accessed 15 February 2018].
- [33] E. Barocio, B. Brenken, A. J. Favaloro, M. Ramirez, J. Ramirez and R. B. Pipes, "Prediction of the Degree of Bonding in the Extrusion Deposition Additive Manufacturing Process of Semi-Crystalline Polymer Composites," in *Science in the Age of Experience*, 2018.
- [34] B. Brenken, E. Barocio, A. J. Favaloro and R. B. Pipes, "Simulation of Semi-Crystalline Composites in the Extrusion Deposition Additive Manufacturing Process," in *Science in the Age of Experience*, 2017.

418

419

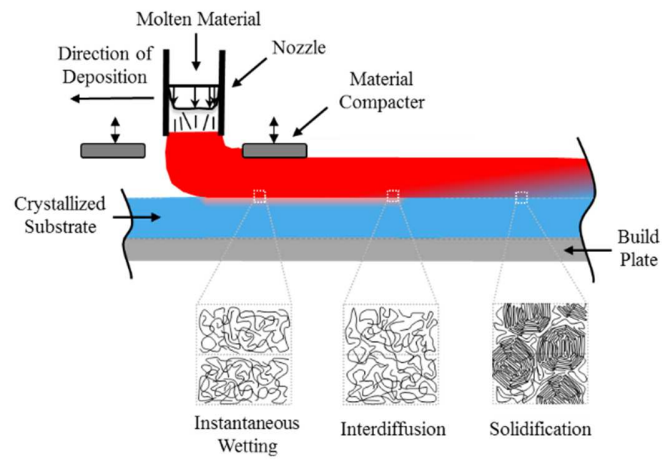


Figure 1. Schematic representation of the ideal conditions for fusion bonding in EDAM with crystallinity developing across the interface between two beads.

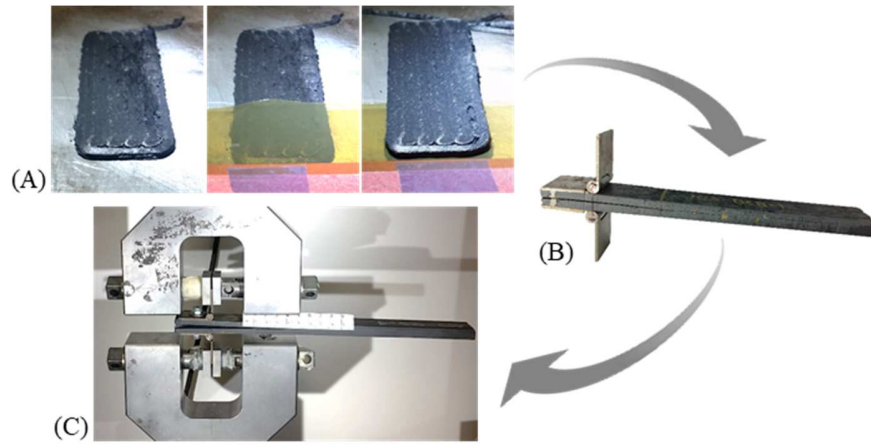


Figure 2. Preparation of DCB bonding experiments. (A) Process of printing panels with initial crack. (B) DCB prepared with piano hinges. (C) Fracture test of DCB.

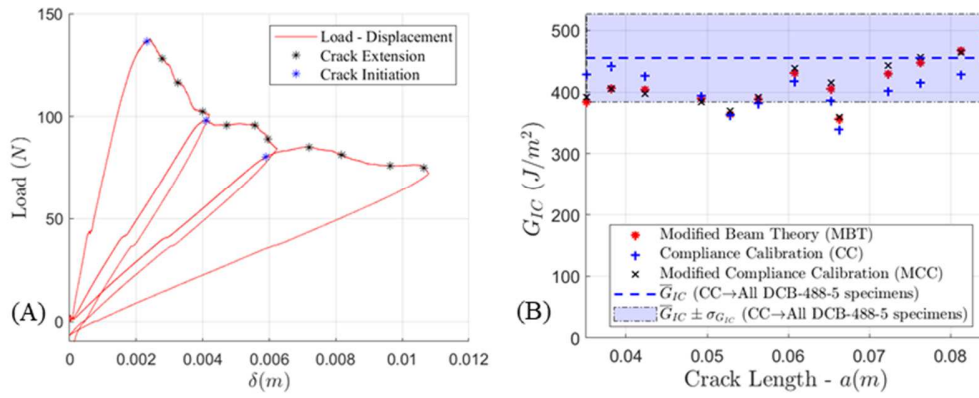


Figure 3. Fracture test of one specimen type DCB-488-5. (A) Load-displacement curve with three loading cycles. (B) Delamination resistance curve.

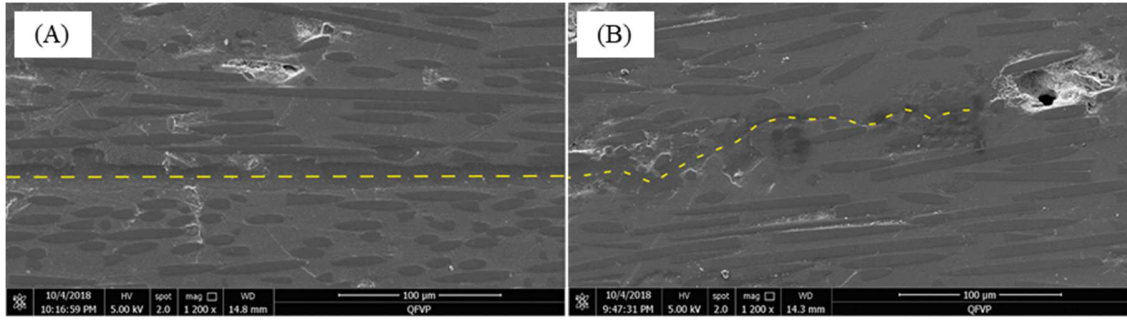


Figure 4. Side view of crack propagation path developed in additively manufactured DCB specimens. (A) Printing condition DCB-393-10. (B) Printing condition DCB-488-5.

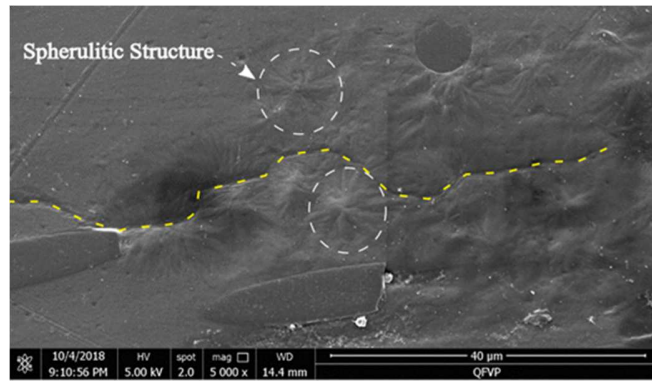


Figure 5. Closer view of the crack propagation path developed in specimen printed with the DCB-488-5 conditions.

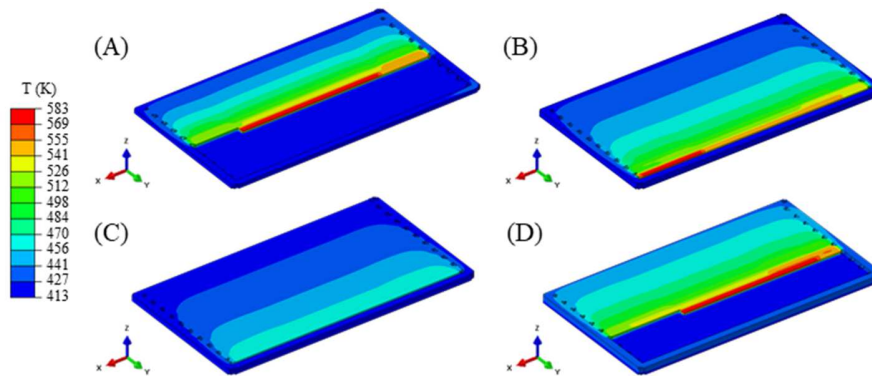


Figure 6. Temperature field developed at different stages in the additive manufacturing process of the panel printed with conditions DCB-413-10. (A) Printing the second layer. (B) End of the third layer. (C) End of dwell time between third and fourth layers. (D) Printing fourth layer after dwell time.

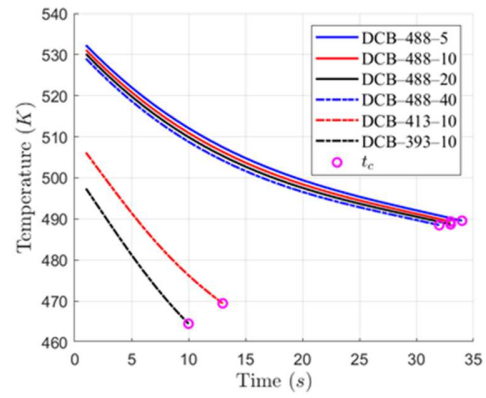


Figure 7. Temperature time histories predicted for each of the bonding experiments until the time to crystallize, t_c .

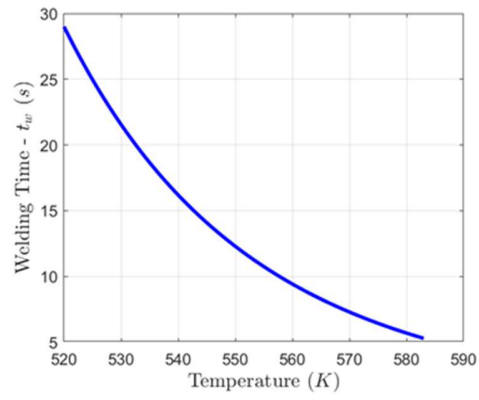


Figure 8. Welding time, t_w , as a function of temperature characterized from bonding experiments.

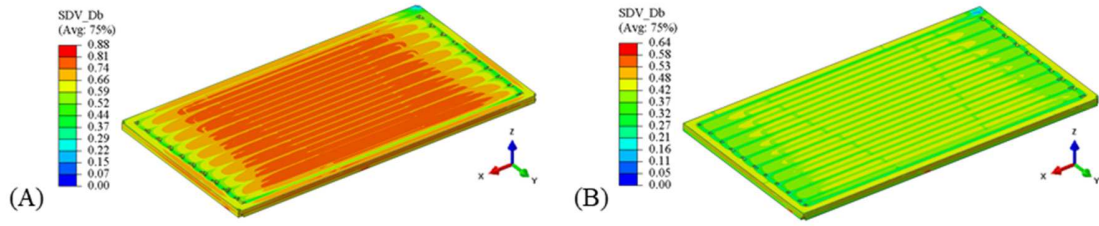


Figure 9. Degree of bonding predicted at the plane of crack propagation in printed panels.
A) Condition DCB-488-10. B) Condition DCB-413-10.

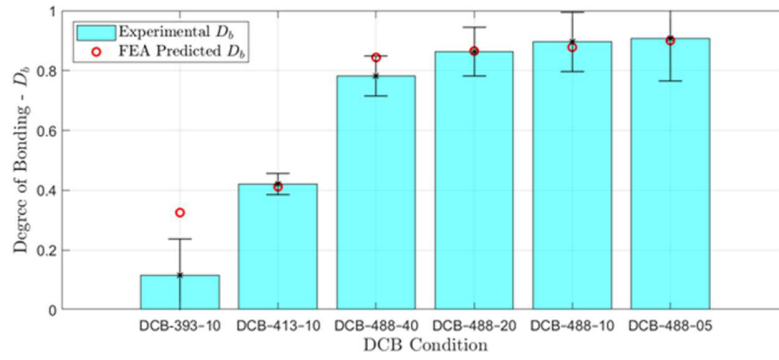


Figure 10. Comparison of the D_b predicted at the plane of crack propagation and the D_b characterized experimentally with error bars indicating one standard deviation.

Table 1. Process conditions used in non-isothermal bonding experiments.

Condition – ID	Build Plate Temperature (K)	Dwell Time (s)
DCB-488-5	488.15	5
DCB-488-10	488.15	10
DCB-488-20	488.15	20
DCB-488-40	488.15	40
DCB-393-10	393.15	10
DCB-413-10	413.15	10
DCB-523-10	523.15	10
DCB-523-10-HT	523.15	10

Table 2. Process conditions used in CAMRI for printing non-isothermal bonding experiments

Process Variable	Value
Bead Dimensions - w, h (mm)	4.7, 1.3
Orifice of Extrusion Nozzle (mm)	3.175
Extrusion Temperature (K)	583.15
Printing Speed (mm/s)	91.67
Tamper Speed ($strokes/s$)	25

Table 3. G_{IC} and degree of bonding measured experimentally.

Condition – ID	Mean G_{IC} (J/m^2)	SD G_{IC} (J/m^2)	Mean D_b	SD D_b
DCB-488-5	455	71	0.91	0.14
DCB-488-10	450	49	0.90	0.09
DCB-488-20	433	40	0.86	0.08
DCB-488-40	392	33	0.78	0.06
DCB-393-10	58	17	0.12	0.03
DCB-413-10	211	60	0.42	0.12
DCB-523-10	502	45	1.0	0.08
DCB-523-10-HT	498	60	–	–

Table 4. Ambient and process conditions utilized for simulating the printing process of panels used in the bonding experiments.

Process Condition	Value
Ambient Temperature Convection (<i>K</i>)	303.15
Ambient Temperature Radiation (<i>K</i>)	423.15
Material Deposition Temperature (<i>K</i>)	583.15
Heat Removed by Compacter (<i>W</i>)	50.0

Table 5. Parameters characterized for the welding time of CF-PPS.

Parameter	Value
E_A (J/mol)	$6.803 \cdot 10^4$
A (s)	$4.258 \cdot 10^{-6}$

Interlayer Fusion Bonding of Semi-Crystalline Polymer Matrix Composites in Extrusion Deposition Additive Manufacturing

